



NGC 6240 supermassive black hole binary dynamical evolution based on *Chandra* data

M. Sobolenko ¹*, O. Kompaniets ^{1,2}, P. Berczik ^{1,3,4}, V. Marchenko ⁵, A. Vasylenko ¹,
E. Fedorova ^{6,7,8} and B. Shukirgaliyev ^{9,10,11}

¹Main Astronomical Observatory, National Academy of Sciences of Ukraine, 27 Akademika Zabolotnoho St, 03143 Kyiv, Ukraine

²Institute of Physics, National Academy of Sciences of Ukraine, 46 av. Nauky, 03028 Kyiv, Ukraine

³Astronomisches Rechen-Institut, Zentrum für Astronomie, University of Heidelberg, Mönchhofstrasse 12-14, D-69120 Heidelberg, Germany

⁴Konkoly Observatory, Research Centre for Astronomy and Earth Sciences, Eötvös Loránd Research Network (ELKH), MTA Centre of Excellence, Konkoly Thege Miklós út 15-17, 1121 Budapest, Hungary

⁵Astronomical Observatory, Jagiellonian University, 171 ul. Orla, PL-30-244 Krakow, Poland

⁶Astronomical Observatory, National Taras Shevchenko University of Kyiv, 3 Observatorna str., 04053 Kyiv, Ukraine

⁷INAF-Osservatorio Astronomico di Roma, via Frascati 33, I-00078 Monte Porzio Catone, Italy

⁸INAF-Osservatorio Astrofisico di Catania, Università di Catania, I-95123 Catania, Italy

⁹Energetic Cosmos Laboratory, Nazarbayev University, 53 Kabanbay Batyr ave, 010000 Nur-Sultan, Kazakhstan

¹⁰Laboratory of Cosmology, Stellar Dynamics and Computational Astrophysics, Fesenkov Astrophysical Institute, 23 Observatory str, 050020 Almaty, Kazakhstan

¹¹Faculty of Physics and Technology, Al-Farabi Kazakh National University, 71 Al-Farabi ave, 050020 Almaty, Kazakhstan

Accepted 2022 August 26. Received 2022 August 26; in original form 2021 October 12

ABSTRACT

The main idea of our research is to estimate the physical coalescence time of the double supermassive black hole (SMBH) system in the centre of NGC 6240 based on the X-ray observations from the *Chandra* space observatory. The spectra of the northern and southern nuclei were fitted by spectral models from Sherpa and both presented the narrow component of the Fe K α emission line. It enabled us to apply the spectral model to these lines and to find relative offset ≈ 0.02 keV. The enclosed dynamical mass of the central region of NGC 6240 with radius 1 kpc was estimated $\approx 2.04 \times 10^{11} M_{\odot}$. These data allowed us to carry on the high-resolution direct N -body simulations with Newtonian and post-Newtonian (up to $2.5\mathcal{PN}$ correction) dynamics for this particular double SMBH system. As a result, from our numerical models, we approximated the central SMBH binary merging time for the different binary eccentricities. In our numerical parameters range, the upper limit for the merging time, even for the very small eccentricities, is still below ≈ 70 Myr. Gravitational waveforms and amplitude-frequency pictures from such events can be detected using pulsar timing array projects at the last merging phase.

Key words: black hole physics – gravitational waves – galaxies: active – galaxies: individual: NGC 6240 – galaxies: kinematics and dynamics – X-rays: galaxies.

1 INTRODUCTION

The model of hierarchical galaxy evolution predicts galactic mergers (White & Rees 1978; Blumenthal et al. 1984; Kauffmann et al. 1999; Menci et al. 2002; Dobrycheva et al. 2018; Zoldan et al. 2019). Since the most observed galactic nuclei harbour the supermassive black holes (SMBHs) in their centre (Richstone et al. 1998; Ferrarese & Merritt 2000; Barausse 2012; Vavilova et al. 2015), the mergers of galaxies nearly always lead to the formation of the binary system of corresponding central SMBHs (Kormendy & Richstone 1995). Their evolution in the interacting galaxies can be described by three basic stages (Begelman, Blandford & Rees 1980).

In gas-free (dry merging) system, the SMBHs become gravitational bound and create SMBH binary (SMBHB) when the semimajor axis approximately equals SMBHB influence radius. It is a sphere radius that contains within the stellar mass equal to double

black hole (BH) mass. The duration of this stage depends on the efficiency of the dynamical friction, but the system definitely forms a pc-scale SMBHB. Afterwards, the SMBHB separation shrinks due to the combined effect of dynamical friction and gravitational slingshot. When the latter process becomes dominating, the binary reaches the hardening phase with a semimajor axis (Quinlan 1996; Yu 2002):

$$a_h \equiv \frac{G\mu}{4\sigma_*^2}, \quad (1)$$

where G is the gravitational constant, the binary reduced mass is $\mu = M_{\text{BH1}}M_{\text{BH2}}/(M_{\text{BH1}} + M_{\text{BH2}})$ with primary and secondary BHs' masses M_{BH1} and M_{BH2} , respectively, and σ_* is the velocity dispersion. The last merging stage is starting as the rapid coalescence of SMBHB via emission of gravitation waves (GWs; Peters & Mathews 1963; Peters 1964a,b; Haehnelt 1994; Wyithe & Loeb 2003; Milosavljević & Merritt 2003a). After coalescence, a single formed SMBH is kicked from the merger remnant centre and is observed as a recoiling SMBH (Campanelli et al. 2007; Choi et al. 2007; González et al. 2007). The accompanying emission of GWs is equivalently taking away up to

* E-mail: sobolenko@mao.kiev.ua

the 10 per cent of total rest-mass of binary system (Reisswig et al. 2009).

SMBHB evolution can be stalled between hardening and GW phases due to depletion of loss cone and merging time is becoming above Hubble time. The so-called ‘final parsec’ problem (Milosavljević & Merritt 2003b) occurs for idealized systems and can be solved in numerical simulations using the self-consistent equilibrium axisymmetric galaxy model (Berczik et al. 2006; Preto et al. 2011), using particles that have multiple encounters with central BHs (Avramov et al. 2021) or using massive perturbers in loss cone (Perets, Hopman & Alexander 2007). Also, the presence of gas in interacting systems (wet merging) plays a significant but unpredictable role, which can decrease or increase the SMBHB merging time depending on system parameters (Cuadra et al. 2009; Lodato et al. 2009; Maureira-Fredes et al. 2018, for recent studies of gas and stars co-influence see Bortolas et al. 2021).

The natural way to search for such SMBHs is by looking at dual or binary active galactic nuclei (AGNs; Husemann et al. 2020). Except for SMBH, the AGN also contains major components such as the accretion disc around the BH and molecular torus (e.g. Ricci et al. 2014; Vasylenko 2018; Gröbner et al. 2020; Kompaniits & Vasylenko 2020). Accretion on to an SMBH is accompanied by converting the gravitational potential energy to the observed radiation, spanning the entire electromagnetic spectrum. Most of this energy dissipates in the innermost few gravitational radii, leading to the bright X-ray emission.

X-ray radiation of AGN commonly is explained by thermal Comptonization of the soft ultraviolet (UV) radiation, produced by the inner parts of the accretion disc in a medium of ‘hot’ electrons around SMBH known as the corona (Haardt & Maraschi 1991, 1993). This radiation (called the primary emission) typically is described by a power-law model and an exponential cut-off at high energies where emission quickly roll-overs (Rybicki & Lightman 1979). Additionally to the continuum is specified the important reflected component, which is the reprocessed primary emission by a cold neutral circumnuclear medium (molecular torus or outer regions of the accretion disc). It is observed as a ‘reflection hump’ at $\sim 20\text{--}30$ keV and emission in Fe $K\alpha$ line at around 6.4 keV (e.g. Matt, Perola & Piro 1991; Mushotzky, Done & Pounds 1993). Due to a combination of abundances and fluorescent yield, the neutral Fe $K\alpha$ at 6.4 keV is typically the strongest emission line seen in AGN’s X-ray spectra. If we found the energy difference for the observed Fe $K\alpha$ lines, we can assume that this shift is due to relative motion between two nuclei at the late stage. That gives the possibility to estimate the mass, enclosed within the common orbit of the binary system (i.e. dynamical mass).

One of the most prominent dual AGN candidates is nearby ultraluminous infrared (IR) galaxy NGC 6240 ($z = 0.0243$, $D_L = 111.2$ Mpc¹) that contains two heavily obscured Compton-thick nuclei separated by $\sim 1''.8$ (Gerssen et al. 2004). Multiple multi-wavelength observations unfold complex morphological structure and confirm that it is in an active merging state (Pasquali, de Grijs & Gallagher 2003). Clearly visible by *Hubble Space Telescope* (HST) irregular elongated morphology of this galaxy is often referred as ‘butterfly’ or ‘lobster-shaped’ (Müller-Sánchez et al. 2018). NGC 6240 is observed as the AGN in X-ray (Komossa et al. 2003; Puccetti et al. 2016; Fabbiano et al. 2020). It shows intensive starburst activity (Barger et al. 1998), supernova explosions of young hot stars (Pignata et al. 2010), and contains H₂O masers (Hagiwara,

Diamond & Miyoshi 2002, 2003). Another interesting property of this galaxy is the presence of the significant amount of dust surrounding the nucleus that causes its high-IR luminosity ($\sim 10^{12}$ L_⊙; see Sanders et al. 2003; Iono et al. 2007).² The Multi-Element Radio Linked Interferometer Network observations at 1.4 and 5 GHz revealed two compact radio sources in the nuclei of NGC 6240 (Beswick et al. 2001). Followed-up high-resolution observations using Very Long Baseline Array and Very Long Baseline Interferometry detected a more complex structure of the central region with several radio sources. Two of the radio sources, namely N1 (northern nucleus, further N) and S (or N2, southern nucleus), matched with compact X-ray sources. The N nucleus may be clearly classified as AGN according to the characteristics in the radio band. The S nucleus spectrum contains composite emission from the AGN and circumnuclear starburst/supernova remnants (Gallimore & Beswick 2004; Hagiwara, Baan & Klöckner 2011). Recently, the results by Kollatschny et al. (2020) and Fabbiano et al. (2020) about the double structure of the S-nucleus are under discussion.

The SMBH mass of the S nucleus lies in the range $(0.87 - 2.0) \times 10^9$ M_⊙ obtained from the high-resolution stellar kinematic results (Medling et al. 2011). Using *K*-band data from *Very Large Telescope* and classical $M_{\text{BH}}\text{--}\sigma$ relation (Tremaine et al. 2002), the N and S nucleus SMBH masses were estimated as $(1.4 \pm 0.4) \times 10^8$ M_⊙ and $(2.0 \pm 0.4) \times 10^8$ M_⊙, respectively (Engel et al. 2010). Engel et al. (2010) traced the motion of the molecular gas by the CO emission and associated it with circular movements. Later, Treister et al. (2010) rather associated it with turbulence motion. Recently obtained with MUSE instrument velocity dispersions correspond to N nucleus BH mass $(3.6 \pm 0.8) \times 10^8$ M_⊙ and combined S (S1 + S2) nucleus BH mass $(8.0 \pm 0.8) \times 10^8$ M_⊙ (Kollatschny et al. 2020).

In the current work, we study the dynamical evolution of the SMBHB system in NGC 6240 using fully parallelized direct *N*-body code $\varphi\text{--GPU}$ (Berczik et al. 2011). This evolution has been examined by performing several simulations of the two SMBHs dynamics, each of which is surrounded by its own bound stellar systems. These simulations required the initial parameters of the binary nucleus in the NGC 6240, which were obtained from spectral analysis of archival *Chandra* observations.

The paper is organized as follows. In Section 2, we present the analysis of X-ray emission from nuclei and dynamical mass estimation. Working code and relativistic treatment of the binary particles are described in Section 3. In Section 4, we describe a physical model and the set of numerical models for the NGC 6240 system based on our BH mass estimation. We applied our results to find the merging time for SMBHB and the expected GWs waveforms from this event in Section 5. Our conclusions are given in Section 6. Throughout this paper, we assume Λ CDM cosmology with a Hubble constant of $H_0 = 70$ km s^{−1} Mpc^{−1}, $\Omega_M = 0.27$, and $\Omega_\Lambda = 0.73$ (Bennett et al. 2003), which gives a scale 1 arcsec = 490 pc (Wright 2006).

2 CHANDRA DATA ANALYSIS

2.1 Image and spectral analysis

NGC 6240 was observed by *Chandra* four times by Advanced CCD Imaging Spectrometer (ACIS) and once by high-resolution camera. In the present work, we used only ACIS observations (ObsID 1590, 6908, 6909, 12713) with a total effective exposure time of

¹<https://ned.ipac.caltech.edu/>

² L_{IR} is the 8–100 μm luminosity.

480.3 ks. The analysis of *Chandra* data was done with the CIAO 4.12 software package (Fruscione et al. 2006) and the calibration data base CALDB 4.9.1. Before the analysis, the data were reprocessed using the `chandra_repro` script recommended in the CIAO analysis threads.

First, the *Chandra* images in different energy bands (0.5–2.5, 2.5–6.0, and 6.0–7.5 keV) were studied for carefully extracting the spectra from the regions corresponding to central BHs. We combined four ACIS observations using the `merge_obs` script from CIAO software package and created the exposure-corrected image (Fig. 1, right). It shows that the neutral Fe $K\alpha$ emission lines were produced only in the central region of the galaxy that accords with the results presented by Komossa et al. (2003).

We restored the image to analyse the detailed spatial structure since the original X-ray data are degraded by the blurring function. To restore the image, we applied the Lucy–Richardson Deconvolution Algorithm implemented in the CIAO tool `arestore`. This algorithm requires an image of point spread function (PSF), which was modelled by the `ChART` and `MARX` programs for detailed ray-trace simulations (Wise 1997; Carter et al. 2003; Fig. 1, left and middle). Consequently, we simulated the PSF for energy $E = 6.25$ keV since we were interested mostly in the analysis of the central part of the galaxy where the emission is dominated by Fe $K\alpha$ line. Two separate nuclei are more clearly visible due to the deconvolution (Fig. 1, middle). Furthermore, the galaxy butterfly-shape in X-ray band matches optical with O III cone, H α bubble, H α filaments, and O III + H α filaments, which are a consequence of galaxies merging history (Müller-Sánchez et al. 2018).

The spectra were extracted from circular regions centred at the centroid position of two bright sources in the galaxy nuclei. Each radius was determined as 3σ encircled count fraction regions of the correspondent PSFs that were separately modelled for the S and N nuclei. The sum of these regions’ diameters is 2 arcsec (≈ 1 kpc) and can be taken as the maximum separation between the nuclei.

For the spectral analysis, we extracted the corresponding spectra from each ObsID using the `specextract` tool from the CIAO software package. The background spectrum was created for a circular region located outside the galaxy and subtracted from nuclei spectra. To take into account the telescope response, we created the Auxiliary Response Files and the Redistribution Matrix Files separately for each ObsID. The spectra of the four ACIS observations for each region were combined using the `combine_spectra` script from CIAO software package. The data were grouped by `group_snr()` to set the minimum value signal-to-noise ratio for each bins and fitted using `SHERPA` (Freeman, Doe & Siemiginowska 2001) fitting application.

The spectra were described in energy range 5.5–7 keV using simple phenomenological model that includes the power-law (`xspowerlw`), Galactic absorption (`xsphabs`), and absorption on the line of sight (`xszphabs`). We also added the Gaussian profiles (`xszgauss`) for the models of the neutral Fe $K\alpha$ fluorescent emission line at 6.4 keV, the He-like iron Fe XXV $K\alpha$ emission line at 6.7 keV and the Fe $K\beta$ fluorescent emission line at 7.08 keV. The photon indices were fixed for nuclei with value $\Gamma = 1.75$. Detailed broadband analysis for continuum spectrum is presented in Puccetti et al. (2016) and Nardini (2017). Finally, the model in `SHERPA` was described as follows:

```
xsphabs * (xspowerlw * xszphabs + xszgauss
           + xszgauss + xszgauss)
```

We compiled the best-fitting parameters in Table 1. The Fe $K\alpha$ best-fitting values are $E_N = 6.41_{-0.02}^{+0.01}$ keV and $E_S = 6.39_{-0.02}^{+0.01}$ keV for N and S nuclei, respectively. Therefore, line shift $\Delta E \approx 0.02$ keV can be interpreted as the result of the motion of each nucleus around the centre of mass. The Fe $K\alpha$ emission lines widths are $\sigma_N = 0.05_{-0.02}^{+0.01}$ keV and $\sigma_S = 0.05_{-0.03}^{+0.04}$ keV for N and S nuclei, respectively. Such values of emission lines widths mean that the Fe $K\alpha$ line is a narrow one. The emission lines at $6.72_{-0.05}^{+0.06}$ and $6.66_{-0.07}^{+0.06}$ keV can be explained as a highly ionized Fe XXV emission from circumnuclear starburst regions (Wang et al. 2014b).

2.2 Mass estimation

Assuming that N and S nuclei have formed the bound system and move around the mass centre, we can estimate the enclosed mass. Based on the energy shift ΔE of the observed Fe $K\alpha$ lines and their line centre mean energy $E_{\text{obs}} = 0.5(E_N + E_S)$ from Table 1, we obtained the velocity shift:

$$\Delta v_{\text{obs}} = \frac{\Delta E c}{E_{\text{obs}}} \approx 937 \text{ km s}^{-1}, \quad (2)$$

where ΔE is the energy shift between two nuclei. We collected velocity differences from other bands in Table 2 and found that in comparison with optical/IR and radio observations, our Δv_{obs} is a factor of three higher. It should be mentioned that this comparison is restricted by several limitations: (i) in most cases, values were obtained after simple visual inspection of velocity maps, which also limited us in velocity error estimations; (ii) different AGNs’ coordinates were used in observations, which complicated maps matching in different bands; (iii) the choice of the region for velocity extraction is unclear and is also complicated by resolutions in different bands (from 0’.5 in X-ray band to 0’.03 in mm band). We assume that this discrepancy can be explained by the model where the X-ray and optic/radio band emission is created in physically different regions at significantly different distances from the central BH.

In the interacting galaxy NGC 6240, we expected that the emission in the Fe $K\alpha$ line would be created on a pc scale (inside the gas-dusty torus; see e.g. Nandra 2006), in contrast with the observed optic/IR emission, which comes from a distance of tens of pc from the central SMBH. Recent studies of bright nearby AGN ($z < 0.5$) with *Chandra* and *XMM-Newton* data are showed that with high probability for 24 objects, the narrow Fe $K\alpha$ line is emitting from the inner 1 pc around SMBH (Andonie et al. 2022). The next generation of planned space-born X-ray observatories includes *Athena* proposed by ESA (Nandra et al. 2013; Barret et al. 2018) and *Lynx* proposed by NASA (The Lynx Team 2018; Gaskin et al. 2019). They are expected to have a higher ~ 100 times spectral resolution on 6 KeV, which can make clear the nature of the observed Fe $K\alpha$ line.

The dynamical mass can be written in terms of observed velocity shift:

$$M_{\text{dyn}} \approx \frac{\Delta R \Delta v_{\text{obs}}^2}{G}, \quad (3)$$

where ΔR is the separation and G is the gravitational constant. Using maximum projected distance $\Delta R_{\text{proj}} = 1$ kpc as a estimation for the minimum physical separation of SMBHB $\Delta R = \Delta R_{\text{proj}}$, we obtained the total dynamical mass within this region $M_{\text{dyn}} \approx 2.04 \times 10^{11} M_{\odot}$. Of course, our dynamical mass estimation is affected by the underlying assumptions about the simple geometry of the NGC 6240 central region. As a first approximation, we assume that



Figure 1. The *Chandra* images of NGC 6240 with the binning factor of 0.5: (left) the original merged image, (middle) the deconvolved image, and (right) the exposure-corrected three-colour image, where colours correspond to energies: red: 0.5–2.5 keV, green: 2.5–6.0 keV, and blue: 6.0–7.5 keV. The yellow line on the right-hand panel is 5 kpc long.

Table 1. The best-fitting parameters for X-ray spectra from northern (N) and southern (S) nuclei.

| Parameter | N | S | Unit |
|--|--|---|-----------------------------------|
| Galactic absorption | 0.0626 ^f | 0.0626 ^f | 10 ²² cm ⁻² |
| Photon index Γ | 1.75 ^f | 1.75 ^f | |
| Absorbing column density N_{H} | 5.00 ^{+0.23} _{-peg} | 31.30 ^{+2.40} _{-2.70} | 10 ²² cm ⁻² |
| Line centre energy Fe $K\alpha$ | 6.41 ^{+0.01} _{-0.02} | 6.39 ^{+0.01} _{-0.02} | keV |
| Line width $\sigma_{\text{Fe } K\alpha}$ | 0.05 ^{+0.01} _{-0.02} | 0.05 ^{+0.04} _{-0.03} | keV |
| Line centre energy Fe XXV | 6.72 ^{+0.06} _{-0.05} | 6.66 ^{+0.06} _{-0.07} | keV |
| Line width $\sigma_{\text{Fe } XXV}$ | 0.01 ^{+0.12} _{-peg} | 0.04 ^{+0.22} _{-peg} | keV |
| Line centre energy Fe $K\beta$ | 7.02 ^{+0.07} _{-0.04} | 7.00 ^{+0.05} _{-0.21} | keV |
| Line width $\sigma_{\text{Fe } K\beta}$ | 0.09 ^{+0.18} _{-0.08} | 0.04 ^{+peg} _{-peg} | keV |
| Reduced $\chi^2/\text{d.o.f}$ | 179.5/175 | 164.1/196 | |

f – marks a fixed parameters, *peg* – indicates a zero error, and *d.o.f* – degrees of freedom.

the projected separation of the nuclei is an intrinsic size of the system. We also assume that the observed velocity shift between nuclei is a real velocity difference. The current simple assumptions we use as a basis for our BHs dynamical merging time estimation at a first order. The detailed parameter study of the possible different orientations and projections of the nuclei we will keep beyond the scope of the current paper.

According to the empirical correlation between SMBH and galaxy bulge masses (Kormendy & Ho 2013), and due to an active merging galaxy state, we estimated the maximum SMBHB total mass $M_{\text{BH}12} = 0.01M_{\text{dyn}} \approx 2.04 \times 10^9 M_{\odot}$. The obtained mean mass M_{BH} is comparable with the dynamical masses previously derived by Medling et al. (2011) and Kollatschny et al. (2020).

The difference ΔE between the Fe $K\alpha$ lines centroids in spectra of both nuclei is the same order as the errors of two line’s positions. Therefore, we performed additional validation of the estimated difference ΔE , using the cross-correlation between N and S nuclei spectra (Fig. 2, left). The cross-correlation between original spectra is presented in Fig. 2 (right), where the magenta line is the fitted Gaussian function. The best-fitting position of the Gaussian profile is 0.0170 ± 0.0019 keV, which is consistent with the estimated shift that we got from spectral fitting within the errors.

3 NUMERICAL MODELLING SMBH PARTICLES

For our simulations, we used our own developed and publicly available φ -GPU³ code, with the blocked hierarchical individual time-step scheme and a fourth-order Hermite integration scheme of the equation of motions for all particles (Berentzen et al. 2008; Berczik et al. 2011). The current version φ -GPU code uses native GPU support and direct code access to the GPU using the NVIDIA CUDA library. The multi-GPU support is achieved through global MPI parallelization. Each MPI process uses only a single GPU, but usually up to four MPI processes per node are started (in order to effectively use the multicore CPUs and the multiple GPUs on our clusters). More details about the φ -GPU code public version and its performance are presented in Khan, Berczik & Just (2018a) and Fiestas et al. (2012). The present code is well-tested and already used to obtain important results in our earlier large-scale (up to few million body) simulations (Li et al. 2012; Zhong, Berczik & Spurzem 2014; Khan et al. 2018b; Wang et al. 2014a). For simulations with lowest particle number $N = 100$ k, we used the GOLOWOOD GPU cluster at MAO NASU. The main part of our numerical experiments with the largest particle number ($N = 500$ and 200 k) we run on the JUWELS GPU cluster of the Jülich Supercomputing Centre.

In the current implementation of the code, we used a post-Newtonian (\mathcal{PN}) formalism for the SMBHB relativistic orbit calculation. In this case, the equation of motion is usually presented as a power series $1/c$ of light velocity, where $n\text{-}\mathcal{PN}$ is proportional to $(v/c)^{2n}$. The acceleration of the i binary particle from a j particle with mass m_j can be written in the following form:

$$\mathbf{a}_i = -\frac{Gm_j}{R^2} [(1 + \mathcal{A}n_{ij}) + \mathcal{B}\mathbf{v}_{ij}], \quad (4)$$

where R is the separation between i and j binary particles, n_{ij} is the normalized position vector, and \mathbf{v}_{ij} is the relative velocity vector. The classic Newtonian acceleration has explicit representation in equation (4), when \mathcal{PN} corrections are contained in two coefficients, \mathcal{A} and \mathcal{B} :

$$\mathcal{A} = \frac{\mathcal{A}_{1\mathcal{PN}}}{c^2} + \frac{\mathcal{A}_{2\mathcal{PN}}}{c^4} + \frac{\mathcal{A}_{2.5\mathcal{PN}}}{c^5} + \mathcal{O}\left(\frac{1}{c^6}\right), \quad (5)$$

³<https://github.com/berczik/phi-GPU-mole>

Table 2. Absolute velocity difference between nuclear regions from X-ray, radio, and optic/IR bands.

| Band | Instrument | Line | Δv km s ⁻¹ | Resolution arcsec | pc | Reference [†] |
|-------|----------------|--|----------------------------------|----------------------|-----|------------------------|
| X-ray | <i>Chandra</i> | Fe K α | 937 | 0.5 | 245 | This paper |
| NIR | SINFONI | CO(2-0) + CO(3-1) | 252 ± 15 | 0.1 | 49 | [1] |
| NIR | SINFONI | H ₂ | 250 | 0.5 | 245 | [2] |
| NIR | SINFONI | [O III] λ 5007 | 150 | 0.5 | 245 | [2] |
| IR | MUSE | Ca II $\lambda\lambda$ 8498, 8542, 8662 | 144 ± 42 | 0.03 | 15 | [3] |
| IR | MUSE | [N II] λ 6548 | 160 ± 54 | 0.03 | 15 | [3] |
| IR | MUSE | [O I] λ 6300 | 262 ± 24 | 0.03 | 15 | [3] |
| Radio | ALMA | CO(3-2) | 250 | 0.3 | 147 | [4] |
| Radio | ALMA | CO(6-5) | 100 | 0.3 | 147 | [4] |
| Radio | ALMA | ¹² CO(2-1) | 300 | 0.03 | 15 | [5] |
| Radio | IRAM | H ₂ | 200 | 0.1 | 49 | [1] |

[†][1] Engel et al. (2010), [2] Müller-Sánchez et al. (2018), [3] Kollatschny et al. (2020), [4] Fyhrie et al. (2021), and [5] Treister et al. (2020).

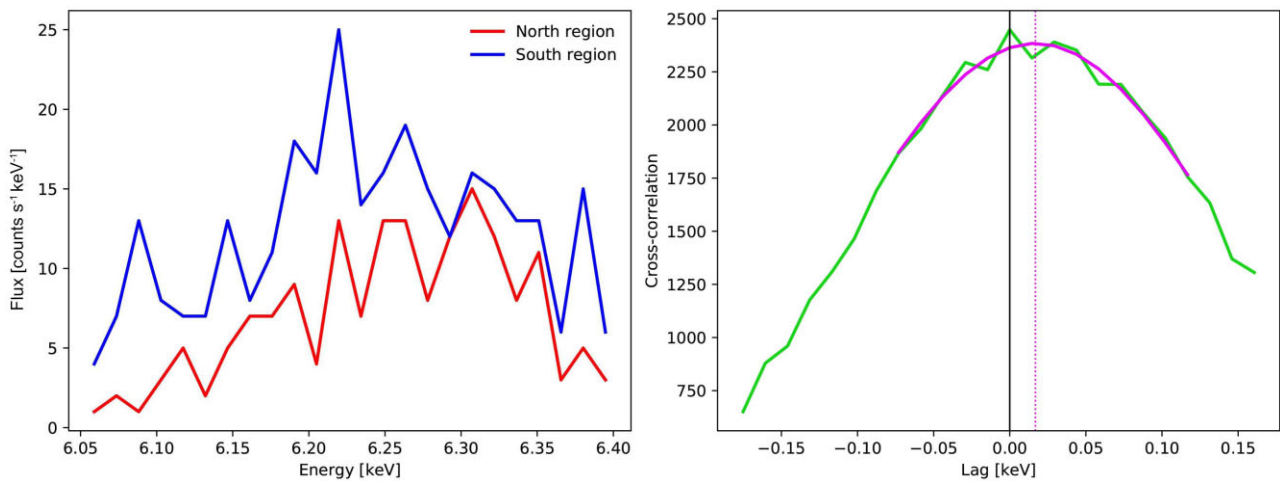


Figure 2. The original X-ray spectra for N and S nuclei (left) and their cross-correlation (right – green line). The magenta curve on the right-hand panel corresponds to a best-fitting Gaussian, where the position of its centre is shown by the magenta dashed line.

$$\mathcal{B} = \frac{\mathcal{B}_{1\mathcal{PN}}}{c^2} + \frac{\mathcal{B}_{2\mathcal{PN}}}{c^4} + \frac{\mathcal{B}_{2.5\mathcal{PN}}}{c^5} + \mathcal{O}\left(\frac{1}{c^6}\right), \quad (6)$$

where $1\mathcal{PN}$ and $2\mathcal{PN}$ are the non-dissipative terms that ‘conserve’ the energy of the system and are revealed in the precession of the orbital pericenter. The $2.5\mathcal{PN}$ is the dissipative term that ‘carries out’ energy from the system due to GWs emission. Coefficients \mathcal{A} and \mathcal{B} are the functions of individual masses, individual velocities, separation, and normalized vector. Their full expressions can be found in Blanchet (2006, equation 168). The detailed references and complete descriptions of the equation of motion in \mathcal{PN} formalism up to $3.5\mathcal{PN}$ can be found at Blanchet (2006), Kupi, Amaro-Seoane & Spurzem (2006), Berentzen et al. (2008), Berentzen et al. (2009), Brem, Amaro-Seoane & Spurzem (2013), and Sobolenko et al. (2017).

A detailed study of the turning on one-by-one \mathcal{PN} corrections shows the requirement to include all \mathcal{PN} terms up to the highest wanted order (Berentzen et al. 2009). Adding conservative $1\mathcal{PN}$ and $2\mathcal{PN}$ corrections remarkably change orbits during three-body encounters and can reduce binary merging time two times. We

applied all \mathcal{PN} corrections up to order $\mathcal{O}(1/c^6)$, so the $2.5\mathcal{PN}$ correction is the highest order that we took into account.

4 SYSTEM INITIAL CONFIGURATIONS

4.1 Physical model and units

The evolution of the central parts of the merging galaxies is closely related to the dynamical processes of the SMBHB evolution. The stars located in the merging galactic centre can interact directly with the SMBHB. Such stars in close orbits around the SMBHB can take away a significant part of the SMBHB angular momentum and energy after the typical three-body gravitational scattering. As a result, the semimajor axis of the binary system monotonically decreases. This process we usually call SMBHB ‘hardening’ (Merritt & Ferrarese 2001; Merritt 2001). The very precise individual orbit calculation of the merging SMBHB in a dense stellar environment gives the correct description of the binary system parameters’ evolution.

We started the galaxy-merger from the dynamical system of two unbound central SMBHBs with a separation $\Delta R = 1$ kpc according to our estimations in Section 2.2 (Table 3). Each SMBHB is surrounded

Table 3. List of parameters for physical model.

| Nucleus | ΔR kpc | M_* $10^{10} M_\odot$ | Q | a pc | M_{BH} $10^8 M_\odot$ | q |
|---------|-------------------|----------------------------|-----|-----------|-----------------------------------|-----|
| (1) | (2) | (3) | (4) | (5) | (6) | (7) |
| 1 (N) | 1 | 13.60 | 0.5 | 200 | 13.60 | 0.5 |
| 2 (S) | – | 6.80 | – | 159 | 6.80 | – |

(1) nuclei ID, (2) initial separation for central BHs, (3) total stellar mass, (4) stellar mass ratio $Q = M_{*2}/M_{*1}$, (5) Plummer radius, (6) masses of the BHs, and (7) mass ratio for the BHs $q = M_{\text{BH}2}/M_{\text{BH}1}$.

by its own bound stellar systems with a simple Plummer density distribution (Plummer 1911):

$$\rho(r) = \frac{3M_0}{4\pi a^3} \left(1 + \frac{r^2}{a^2}\right)^{-\frac{5}{2}}, \quad (7)$$

which produce the cumulative mass distribution:

$$M(< r) = M_0 \frac{r^3}{(r^2 + a^2)^{3/2}}, \quad (8)$$

where M_0 is the total mass of each galactic bulge and a is a scale factor that characterizes the size of each nucleus (Plummer radius). Due to the flat central distribution of the Plummer profile, the SMBHB hardening as the assuming numerical hardening will be smaller compared to the more peaked core distribution profiles (Jaffe 1983; Hernquist 1990; Dehnen 1993). Using the Plummer distribution, we model the minimum numerical hardening for our SMBHB.

Previously estimated from observations, dynamical mass is assumed as the total mass of the stellar component $M_{*,\text{tot}} = M_{\text{dyn}} = 2.04 \times 10^{11} M_\odot$. Corresponding to Section 2.2, the mass of the SMBHB is set $M_{\text{BH}12} = 2.04 \times 10^9 M_\odot$. Supposing the major merging we used for the mass ratio of the galactic bulges and the central BH's 2:1 ratio. According to this assumption, the primary (heavier) bulge with mass $M_{*1} = 1.36 \times 10^{11} M_\odot$ contains BH with mass $M_{\text{BH}1} = 1.36 \times 10^9 M_\odot$ and secondary (lighter) bulge with mass $M_{*2} = 6.8 \times 10^{10} M_\odot$ contains BH with mass $M_{\text{BH}2} = 6.8 \times 10^8 M_\odot$ (Table 3). Also for further reference we calculated the Schwarzschild radius of the SMBHB as $R_{\text{SW}12} = 2GM_{\text{BH}12}/c^2 = 195 \mu\text{pc}$.

For the first bulge, we assumed the Plummer radius to be near equal to the influence radius of the BH, which gives $a_1 = 0.2\Delta R = 200$ pc. For the second (smaller) bulge, we set the Plummer radius proportionally smaller, assuming the same central density in both bulges, that is, $a_2 = 0.5^{1/3}a_1 \approx 159$ pc (Table 3). The initial orbital velocities of the merging galactic bulges (together with the BH's) are set such that the orbital eccentricity (in point-mass approximation) equals $ecc_0 = 0.5$.

For the numerical scaling, we used the N -body normalization (Hénon 1971).⁴ The physical units were chosen according to estimations for total stellar mass and maximum projected separation between BHs:

$$M_{\text{NB}} = M_{\text{dyn}} = 2.04 \times 10^{11} M_\odot, \quad (9)$$

$$R_{\text{NB}} = \Delta R = 1 \text{ kpc}. \quad (10)$$

In the N -body system of units, we have for velocity and time units the rescaling values:

$$V_{\text{NB}} = 936.7 \text{ km s}^{-1}, \quad (11)$$

⁴https://en.wikipedia.org/wiki/N-body_units

Table 4. List of parameters for basic and mass prescription numerical models.

| N | RAND | $m_{\text{HMP}}:m_{\text{LMP}}$ | m_{HMP} $10^6 M_\odot$ | m_{LMP} $10^6 M_\odot$ | \mathcal{PN} |
|-------|---------|---------------------------------|------------------------------------|------------------------------------|----------------|
| (1) | (2) | (3) | (4) | (5) | (6) |
| 100 k | 1, 2, 3 | 10:1 | 10.20 | 1.130 | 1 |
| 200 k | 1, 2, 3 | 10:1 | 5.10 | 0.567 | 2 |
| 500 k | 1, 2, 3 | 10:1 | 2.04 | 0.227 | 3 |
| 100 k | 1 | 1:1 | – | 2.400 | – |
| 100 k | 1 | 5:1 | 5.10 | 1.280 | – |
| 100 k | 1 | 20:1 | 20.40 | 1.070 | – |

(1) Total number of particles, (2) randomization seed number, (3) HMPs-to-LMPs mass ratio, (4 and 5) mass of HMPs and LMPs, respectively, and (6) randomization seed number for which we turned \mathcal{PN} correction.

$$T_{\text{NB}} = 1.04 \text{ Myr}. \quad (12)$$

In this system of units (Sobolenko et al. 2017), we got the value for the light speed: $c = 320 V_{\text{nb}}$.

4.2 Numerical models

To check the numerical convergence of our Newtonian dynamical ‘hardening’ time-scale results, we used three different total particle numbers for the system, $N = 100\text{k}$, 200k , and 500k . For each of these particle numbers, we ran a separate set of simulations with three different particle random seeds, $\text{RAND} = 1, 2, \text{ and } 3$ (Table 4, top three numerical models). Below we will use the abbreviation 100–1 for a run with particle number $N = 100\text{k}$ and random seed $\text{RAND} = 1$. In all of these nine basic runs, we generated two different types of particles for each galaxy (completely mixed inside the system), the so-called ‘high mass’ (HMPs) and ‘low mass’ particles (LMPs). We fixed the individual particles’ mass ratio for these particles as 10:1. For all the nine runs, we also used the fixed number ratio for the HMPs and LMPs particle number: $N_{\text{HMP}}:N_{\text{LMP}} = 1:10$. This small fraction of HMPs allowed us to mimic the dynamical influence of the giant molecular clouds and/or the compact stellar systems (globular clusters) on the common stellar system of the merging centres (colliding bulges). Even this small fraction of ‘super’ particles with a larger gravitational softening can have a great influence on the phase space mixing of the ‘normal’ stellar particles.

We also run three additional runs with $N = 100\text{k}$ simulations using the different HMPs to LMPs individual mass ratio. In comparison to the basic runs, where we set the ratio 10:1, we run simulations with mass ratios 5:1, 20:1 and with just LMPs without HMPs 1:1 (Table 4, bottom three models). We specially carried out these three runs to illustrate the dynamical effect of the possible higher-mass ratio of the particles.

For different number of particles, we also set a different individual gravitational softening length. For the BH–BH particles interaction, we used the exactly zero softening ($\epsilon_{\text{BH}} = 0.0$). For the HMPs, we used $\epsilon_{\text{HMP}} = 10^{-4} R_{\text{NB}} = 0.1$ pc gravitational softening. For the LMPs, we set $\epsilon_{\text{LMP}} = 10^{-5} R_{\text{NB}} = 0.01$ pc. For the mixed interactions between the different type of particles, we used the mixed gravitational softening between the particles:

$$\epsilon_{ij}^2 = 0.5 (\epsilon_i^2 + \epsilon_j^2). \quad (13)$$

In a case, if one of the particles is a BH (or i or j), we set the additional coefficient 10^{-2} in front of the equation (13) to make a further

Table 5. Time-scales for models with turned on \mathcal{PN} terms.

| N | RAND | t_b Myr | $t_{\mathcal{PN} \text{ beg}}$ Myr | t_{merge} Myr |
|-------|-------------------|--------------|---------------------------------------|---------------------------|
| (1) | (2) | (3) | (4) | (5) |
| 100 k | 1 | 3.77 | 10.4 | 43.6 |
| 200 k | 2 | 3.90 | 10.4 | 34.7 |
| 500 k | 3 | 3.77 | 10.4 | 30.5 |
| 500 k | A.18 ^a | 5.15 | 23.5 | 40.3 |
| 500 k | A.25 ^a | 5.15 | 32.7 | 46.7 |

(1) Total number of particles, (2) randomization seed number for which we turned \mathcal{PN} correction, (3) binding binary time, (4) time for turning \mathcal{PN} correction, and (5) merging time. ^aModel A from S21.

extra reduction for such a gravitational interaction. As the result, we obtained effective softening parameters in level $10^{-5} R_{\text{NB}} = 0.01$ pc and $10^{-6} R_{\text{NB}} = 0.001$ pc for HMPs and LMPs, respectively.

Leaned on the nine basic Newtonian runs, we run three full \mathcal{PN} runs to leading SMBHB to merging, where we turned on the extra \mathcal{PN} terms for the BH–BH gravitational interaction. Specially chosen, three different Newtonian runs have different particle numbers and are noted with a suffix \mathcal{PN} (Table 4, top three numerical models). The \mathcal{PN} terms turned on time $t_{\mathcal{PN} \text{ beg}} \approx 10$ Myr after the binary binding at time t_b (Table 5). We stopped these runs when the SMBH particles separation fell below $\approx 4 R_{\text{SW12}}$ and this time assumed as merging time t_{merge} (Table 5). We will also compare our results with previous simulations, which consist of 4 physical and 16 numerical models (Sobolenko, Berczik & Spurzem 2021, hereafter S21).

5 SIMULATION RESULTS AND DISCUSSION

5.1 Dynamical time-scales

We describe the evolution of the SMBHB by the evolution of the binary orbit’s parameters, such as separation ΔR , inverse semimajor axis $1/a$, and eccentricity ecc (Fig. 3). As mentioned above, at time $t = 0.0$ Myr, the SMBH particles at initial separation ΔR are not bound. In the Newtonian N -body simulations, the binary forms after several passages at binding time t_b in less than 4 Myr (Tables 5 and 6). The evolution of separation (Fig. 3, top) and inverse semimajor axis (Fig. 3, middle) shows a quite good agreement for a different number of particles and initial randomization of N -body particles’ positions and velocities. This already made the results of our simulations quite independent from these purely numerical parameters. In comparison with model A (the closest model for our current research from S21), current basic numerical models show an earlier (≈ 20 per cent) binding time t_b (Table 5). In our set of runs, the bound binary is usually formed with a semimajor axis almost equal to the SMBHs influence radius.

For basic numerical models, the eccentricity did not show any systematic dependence on the number of particles or randomization seeds due to their very ‘stochastic’ nature. In the basic models with 100 k particles, the binaries were formed with eccentricities from 0.84 to 0.94. For the basic 200 k runs, we get the eccentricities in the range 0.42–0.88. For the basic 500 k runs, we get an even wider range 0.34–0.92 (similar to in S21). To make our conclusion more statistically significant, we performed additional Newtonian N -body simulations for $N = 100\text{k}$, 200k, and 500 k with different randomization seeds, and as a result, we have 14 runs for each N .

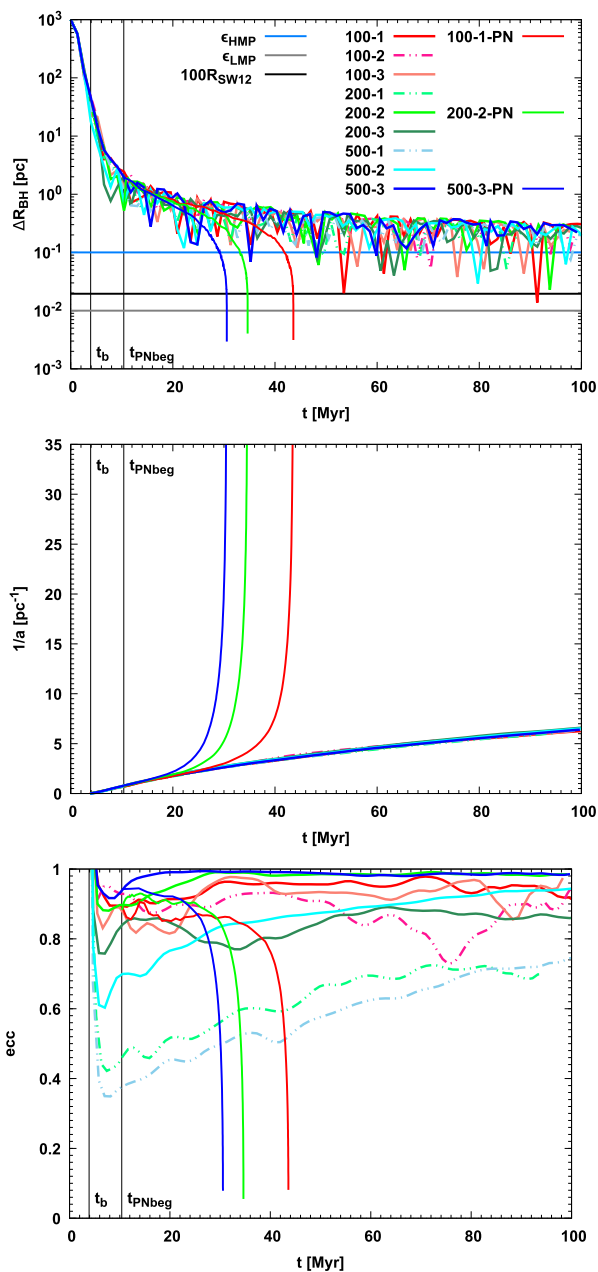


Figure 3. Evolution of SMBHB separation (top), inverse semimajor axis (middle), and eccentricity (bottom) for basic Newtonian (colour dashed lines) and \mathcal{PN} runs (colour solid lines) with mass ratios HMPs to LMPs 10:1 from Table 4. The red, green, and blue solid lines are \mathcal{PN} runs for particle number 100, 200, and 500 k, respectively. On the top panel, the horizontal solid light blue and grey lines are softening parameters for HMPs and LMPs, respectively, the solid black line is 100 Schwarzschild radii. Vertical black dashed lines are binding time t_b for models 100–1, 200–2, and 500–3 (Table 5) with following turning on \mathcal{PN} terms at time $t_{\mathcal{PN} \text{ beg}}$ (Table 5).

SMBHs orbits show a smooth trend with the orbital eccentricity higher than 0.5 (Fig. 4). The orbital eccentricity slightly grows during the binary evolution (Preto et al. 2011). In Fig. 4, we present the cumulative eccentricity distribution for the three characteristic times (bounding time; time, when \mathcal{PN} terms turn on; a time when the hard binary forming). We do not have a substantial dependence on the particle numbers N . Our N -independent wide eccentricity range (0.40–0.99) for the binaries does not really support the predictions

Table 6. Time-scales for additional numerical models with $N = 500$ k and different randomization seeds.

| RAND | t_b Myr | t_h Myr | t_{merge} Myr |
|------|--------------|--------------|---------------------------|
| (1) | (2) | (3) | (4) |
| 4 | 4.10 | 14.04 | 38.4 |
| 5 | 4.13 | 14.95 | 40.0 |
| 6 | 4.10 | 14.60 | 15.2 |
| 7 | 4.04 | 12.87 | 19.1 |
| 8 | 4.03 | 13.40 | 24.7 |
| 9 | 4.10 | 15.34 | 27.2 |
| 10 | 4.16 | 14.69 | 46.0 |
| 11 | 3.87 | 13.91 | 20.9 |
| 12 | 4.16 | 14.04 | 56.8 |
| 13 | 4.06 | 14.30 | 38.1 |

(1) Randomization seed number for which we turned \mathcal{PN} corrections, (2) binding binary time, (3) form hard binary time, and (4) merging time.

of a more narrow eccentricity spread as an increasing number of N -body particles (Rantala et al. 2017; Nasim et al. 2020).

After turning on the \mathcal{PN} terms at time $t_{\mathcal{PN}\text{beg}} = 10 T_{\text{NB}} = 10.04$ Myr, all our \mathcal{PN} runs show a quite short dynamical merging time t_{merge} comparable with obtained by Khan et al. (2016), Khan et al. (2018b; Table 5). Basically all three different \mathcal{PN} models (100–1, 200–2, and 500–3) merge in under ≈ 44 Myr (Table 5). Differences at the merging times can be explained by the strong effect of the eccentricities at the time when we turned on \mathcal{PN} corrections. A previous detailed study of 20 physical and numerical models showed that the merging time for central SMBHB is less than 50 Myr (for full description see S21). But our current binary models can merge even earlier around 31 Myr (model 500–3), which can be explained by a higher eccentricity (≈ 0.9) at the binary formation time than in S21.

To check the merging time dependency of our PN runs from the different randomization seeds (RAND) for the particle distributions, we carry out extra 10 runs of the 500-3-PN model (Table 6). Before starting the extra PN runs, we estimated the bounding time $t_b \approx 4$ Myr and hardening time $t_h \approx 15$ Myr for each run. The SMBHB merging time varies in a range from 15.2 to 56.8 Myr and, as we expect, mainly depends on the initial eccentricity after the moment of the binary formation (Fig. 5). From our limited sample (totally 11 \mathcal{PN} simulations), we already can conclude that the merging time can be approximated as a quite shallow function of the eccentricity:

$$t_{\text{merge}} = A \times [1 - (ecc_{10})^{27}]^B, \quad (14)$$

where coefficients $A = 71.98 \pm 7.89$ and $B = 0.46 \pm 0.07$. As a basic conclusion from these extra 10 runs, we can state that even for the very small initial eccentricity the merging time has the upper limit around ≈ 70 Myr.

In the Fig. 6, we show the results from our extra runs with 100 k particles (Table 4, tree bottom models), which we started to check the effect of different HMPs-to-LMPs mass ratios ($m_{\text{HMP}}:m_{\text{LMP}} = 20:1, 10:1, 5:1, \text{ and } 1:1$). Our runs with mass prescriptions show a qualitatively similar evolution in separation, inverse semimajor axis, and even eccentricity. For the inverse semimajor axis $1/a$ (Fig. 6, middle), we see the trend that is more significant at time ≈ 100 Myr. This trend strongly depends on the limit close to the 1:1 particles mass ratio and is determined by the mass of LMPs (see Table 4 for

m_{LMP}). Because we always have a larger amount of LMPs (i.e. more interaction with the LMP particles), the binary hardening always more strongly depends on the LMPs masses. The small amount of HMPs (≈ 9 per cent), in each mass prescription model, apparently is not enough for extracting sufficient energy amount during three-body encounters with the binary SMBH. For a quantitative description of this process, a detailed study of energy balance is required (for example as it was made by Avramov et al. 2021).

For mass prescription models, the eccentricity (Fig. 6, bottom) varies in a narrower range 0.85–0.99 than for basic numerical runs (Fig. 3, bottom). We do not see any strong dependence of the binary initial eccentricity from the LMPs particles individual masses. Lines for different models are very often overlapping (crossing). We can just note that models with higher mass ratios (20:1, 10:1) have some kind of ‘bumps’. This can indicate the interaction with the particular HMP. Even if their number is much lower compared to the LMP, such a small number of high mass field particles can play a significant role in the binary eccentricity behaviour.

5.2 Gravitational waves

For our model with maximum N and turning on \mathcal{PN} terms ($N = 500$ k, RAND = 3, $m_{\text{HMP}}:m_{\text{LMP}} = 10:1$), we also calculated the expected amplitude-frequency picture for SMBHB merging in NGC 6240. For the simple waveform calculation, we used the GW quadrupole term expressions from Kidder (1995; also see Brem et al. 2013; Sobolenko et al. 2017):

$$h^{ij} = \frac{2G\mu}{D_L c^4} [Q^{ij} + P^{0.5} Q^{ij} + P Q^{ij} + P^{1.5} Q^{ij} + \dots], \quad (15)$$

where P is a correction term for corresponding \mathcal{PN} order, μ is the reduced mass, D_L is the luminosity distance between the origin of the reference frame and the source, and Q^{ij} is the quadrupole term. The last one can be written in the form:

$$Q^{ij} = 2 \left[v^i v^j - \frac{GM_{\text{BH}12}}{r} n^i n^j \right], \quad (16)$$

where v^i and n^i are the relative velocity and normalized position vectors in this reference frame, respectively.

For illustrative purposes, we did not use highly accurate model waveforms and neglected the higher order terms. In this assumption, we calculated the tensor in the source frame simply by:

$$h^{ij} \approx \frac{4G\mu}{D_L c^4} \left[v^i v^j - \frac{GM_{\text{BH}12}}{r} n^i n^j \right]. \quad (17)$$

For the sake of simplicity, we choose the virtual detector to be oriented such that the coordinate axes coincide with the source frame. It allowed us to not make any coordinate transformations. We computed h_+ and h_\times from h^{ij} , which gave the relevant measurable strains in ‘+’ and ‘ \times ’ polarizations (Brem et al. 2013; Sobolenko et al. 2017).

The standard resolution for our \mathcal{PN} runs was 1.3×10^5 yr. We extracted the SMBH particles data (positions & velocities) from the last available \mathcal{PN} model’s snapshot to calculate the final stage of the SMBH merger (up to $\approx 4R_{\text{SW}12}$) with the high resolution. Using these particle data, we followed only the two SMBHs dynamical \mathcal{PN} evolution. For this purpose, we used our highly accurate two-body Hermite integrator. We run these separate simulations with the maximum possible accuracy, keeping at minimum 100 points per SMBH particles orbital integration, which give us time resolution up to ~ 3 d.

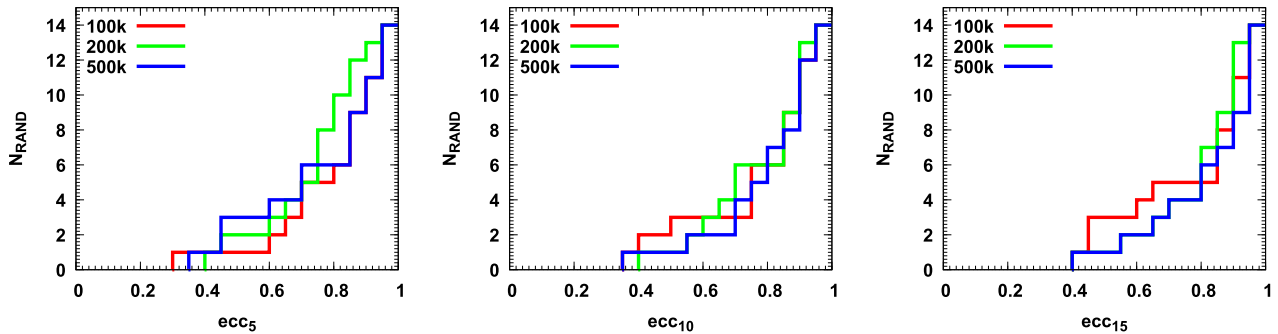


Figure 4. Eccentricity cumulative distributions for numerical models with different randomization seeds (RAND) at different times from left to right: $t = 5.2$ Myr (5 NB; bounding time), 10.4 Myr (10 NB; turning \mathcal{PN} terms), and 15.6 Myr (15 NB; forming hard binary). Colour show models with the different number of particles N : red – 100k, green – 200k, and blue – 500k.

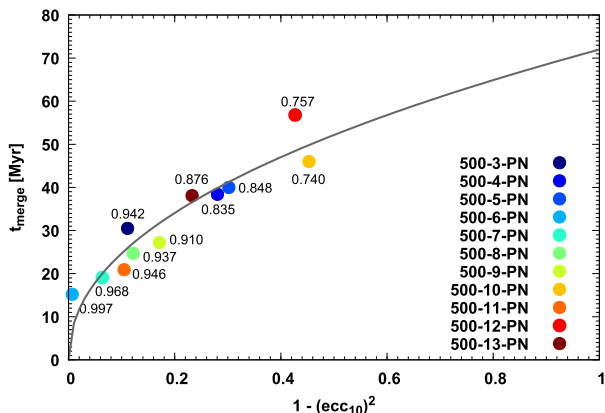


Figure 5. SMBHB merging time as function of eccentricity at time $t = 10.4$ Myr (10.0 NB), when we started \mathcal{PN} runs. Colour show models with different randomization seeds RAND and numbers show the eccentricity values. Grey dashed line is fitting function (see equation 14).

The calculated waveforms for h_+ polarization and amplitude-frequency picture from the final phase of our model runs (last 50 yr and zoomed last 10 yr evolution before the merger) are presented in Fig. 7. It is worth noting that \mathcal{PN} approximation works well for describing the early inspiral SMBHBs, and numerical relativity and perturbation theory should be used for full waveforms picture of merging event and ringdown (for reference see Le Tiec 2014). Obtained frequencies for merging events from such high-mass SMBHBs ($\sim 10^{8-9} M_\odot$) at such distances ($D_L = 111.2$ Mpc) lay on sensitive curve of current and future pulsar timing array (PTA) consortium’s: European PTA (Kramer & Champion 2013), Parkes PTA (Hobbs 2013), North American Nanohertz Observatory for Gravitational Waves (NANOGrav; Ransom et al. 2019), which collectively form International PTA (IPTA; Manchester & IPTA 2013). Such detection of individual SMBHBs merging and GWs stochastic background (see the recent NANOGrav 12.5 yr data set results at Arzoumanian et al. 2020) will be a strong evidence of the possibility of SMBHBs binding, their reaching sub-pc scale, merging, and emitting GWs.

6 CONCLUSIONS

In this paper, we investigated the X-ray properties of dual AGN in NGC 6240 using *Chandra* observations in the 0.5–7.5 keV and performed numerical N -body simulations based on the results of the

corresponding spectral analysis. The main conclusions of this study can be summarized as follows.

(i) We performed X-ray analysis of the combined spectrum from four *Chandra* observations of NGC 6240 with resulting exposure of 480 ks for each of two active nuclei. These spectra demonstrated individual Fe $K\alpha$ emission lines with observational energies $E_S = 6.39^{+0.01}_{-0.02}$ keV and $E_N = 6.41^{+0.01}_{-0.02}$ keV, with corresponding line widths $\sigma_S = 0.05^{+0.04}_{-0.03}$ keV and $\sigma_N = 0.05^{+0.01}_{-0.02}$ keV for South and North nuclei, respectively.

(ii) We estimated the dynamical mass for these nuclei as $M_{\text{dyn}} \approx 2.04 \times 10^{11} M_\odot$ from X-ray analysis, assuming that obtained energy shift caused by the relative motion of the two nuclei at the late stage. Accepting that this mass represents the mass of bulge, we estimated SMBHB mass as $M_{\text{BH12}} \approx 2.04 \times 10^9 M_\odot$. This value is comparable with estimations by other authors (Medling et al. 2011; Kollatschny et al. 2020).

(iii) Based on the estimated bulge mass and maximum projected separation $\Delta R = 1$ kpc of the central SMBHB, we constructed a physical model of the merging system. Using this physical model, we made 12 basic numerical models’ realizations with different particles number $N = 100, 200$, and 500k. To obtain the merging time, we run Newtonian and \mathcal{PN} N -body models (up to $2.5\mathcal{PN}$ term). As a basic code, we used our own direct N -body φ –GPU code with fourth-order Hermite integration scheme and individual time-steps for particles.

(iv) All basic Newtonian simulations showed a very good alignment in inverse semimajor axis evolution. From these runs, we concluded the independence of our SMBHB hardening results on the initial number of particles (100, 200, and 500k) and randomization for particles’ positions and velocities. The eccentricity did not show any systematic dependence neither on the number of particles nor randomization seeds due to its very ‘stochastic’ nature.

(v) To make our conclusions more statistically significant, we performed extra Newtonian N -body simulations for $N = 100, 200$, and 500k with different randomization seeds. For extra simulations, eccentricity also did not show any substantial dependence on the particle numbers N . Our N -independent wide eccentricity range (0.40–0.99) for the binaries does not support the predictions (Rantala et al. 2017; Nasim et al. 2020) of a more narrow eccentricity spread as an increasing number of N -body particles.

(vi) To estimate the merging time for a central SMBHB, we combined the basic Newtonian and \mathcal{PN} numerical models. The obtained merging times lay in a range from 15 to 57 Myr, which is in a quite good agreement with our previous results (Sobolenko,

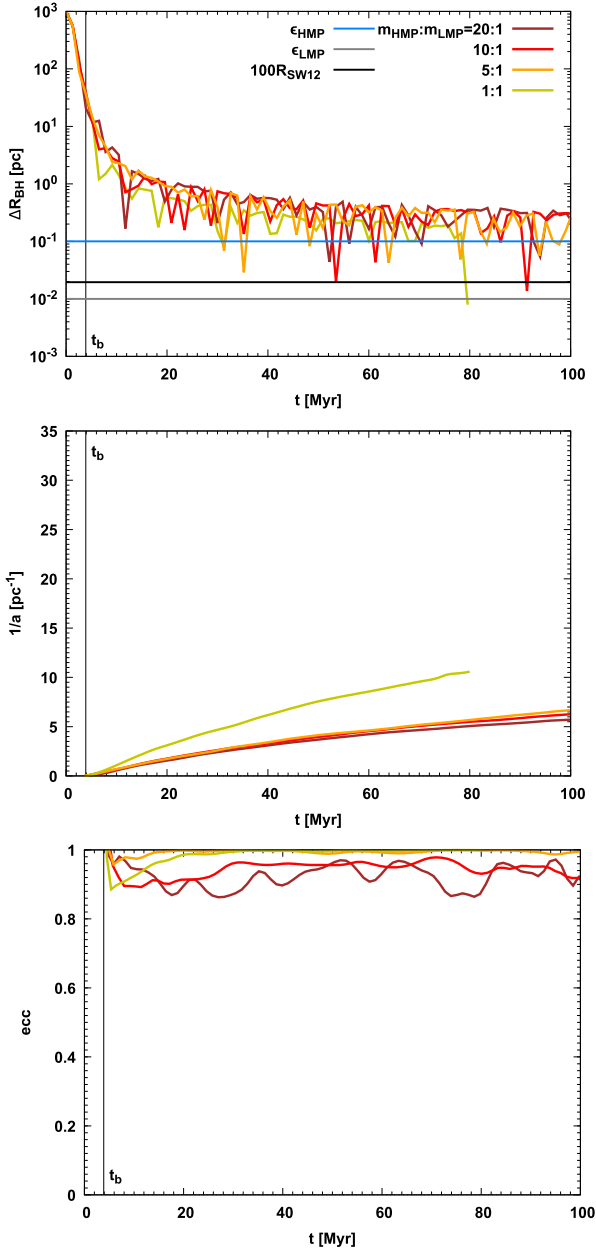


Figure 6. Evolution of SMBHB separation (top), inverse semimajor axis (middle), and eccentricity (bottom) for Newtonian runs (dashed lines) with number of particles $N = 100\text{ k}$, randomization seed $\text{RAND} = 1$, and different mass ratios HMPs to LMPs $m_{\text{HMP}}:m_{\text{LMP}} = 20:1, 10:1, 5:1, 1:1$ from Table 4. On the top panel, the solid light blue and grey lines are softening parameters for HMPs and LMPs and the solid black line is 100 Schwarzschild radii. The vertical black dashed line is binding time t_b for models (Table 5).

Berczik & Spurzem 2016; Sobolenko et al. 2021). The extra 10 \mathcal{PN} Newtonian and \mathcal{PN} models with $N = 500\text{ k}$ and different randomization seeds for the particle distributions also show a quite similar result. Based on the numerical approximation of the merging time as a function of SMBHB eccentricity, we can conclude that even for the possibly very small initial eccentricity, the merging time anyway has an upper limit around ≈ 70 Myr.

(vii) Implementing relativistic \mathcal{PN} approximation up to $2.5\mathcal{PN}$ terms allowed us to follow the SMBHB evolution till the mpc scale. We obtained the waveforms and amplitude-frequency maps for the

last 50 and 10 yr for the SMBHB system in interacting galaxy NGC 6240. Such SMBHBs merging events can be observed in the current and future PTA campaigns.

The presented complete research, from observation analysis to numerical modelling, gives us a powerful key for detailed investigation of complex objects such as double/multiple AGN systems at different merging stages.

ACKNOWLEDGEMENTS

The authors thank the anonymous referee for the fruitful comments and corrections of our mistakes/typos in the manuscript. We believe that her/his useful comments greatly improved the final version of our paper.

The authors gratefully acknowledge the Gauss Centre for Supercomputing (GSC) e.V. (www.gauss-centre.eu) for funding this project by providing computing time through the John von Neumann Institute for Computing (NIC) on the GCS Supercomputers JURECA and JUWELS at Jülich Supercomputing Centre (JSC). This research has made use of data obtained from the Chandra Data Archive and the Chandra Source Catalog, and software provided by the Chandra X-ray Center (CXC) in the application packages CIAO and SHERPA.

OK is grateful to Dr O. Torbaniuk for his useful discussions and comments and Dr. I. Vavilova for helpful remarks. OK acknowledge support by the budgetary program ‘Support for the development of priority fields of scientific research’ (CPCEL 6541230), project No. 10-F, and the Target Complex Program of Scientific Space Research of the National Academy of Sciences of Ukraine. OK thanks the Astronomical Observatory of the Jagiellonian University for support during the International Summer Student Internship, where a part of this work was done.

The work of VM was supported by the Polish National Science Centre grant 2016/22/E/ST9/00061.

MS acknowledges the support under the Fellowship of the National Academy of Sciences of Ukraine for young scientists 2020-2022. PB and MS acknowledge support by the Volkswagen Foundation in Germany under the grant no. 97778. The work of PB was also supported by the Volkswagen Foundation under the special stipend no. 9B870 (2022).

PB and BS also acknowledges the support from the Science Committee of the Ministry of Education and Science of the Republic of Kazakhstan (grant no. AP08856149). PB thanks the support by Ministry of Education and Science of Ukraine under the France - Ukraine collaborative grant M2-16.05.2022. PB express acknowledge the support by the National Academy of Sciences of Ukraine under the Main Astronomical Observatory GPU computing cluster project no. 13.2021.MM.

The work of PB, AV, and MS was supported under the special program of the National Research Foundation of Ukraine ‘Leading and Young Scientists Research Support’ – ‘Astrophysical Relativistic Galactic Objects (ARGO): life cycle of active nucleus’, no. 2020.02/0346.

BS acknowledges the Nazarbayev University Faculty Development Competitive Research Grant Program no. 11022021FD2912 (ssh2022007).

DATA AVAILABILITY

The data underlying this article will be shared on reasonable request to the corresponding author.

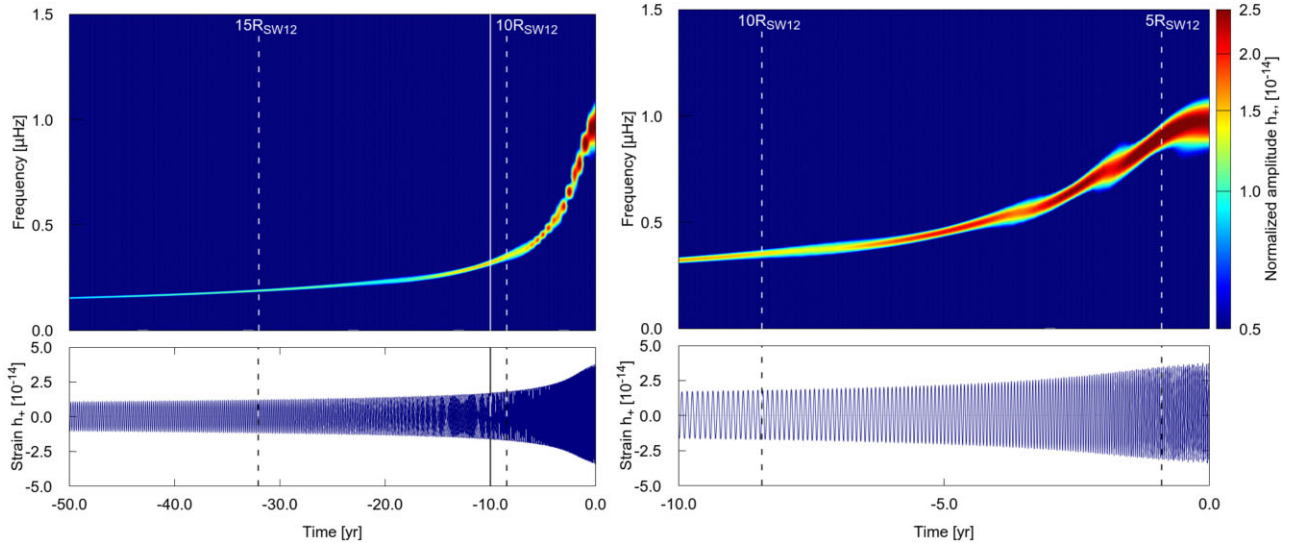


Figure 7. Time-frequency representations (top) of the strain data (bottom) for predicted gravitational waveforms of h_+ polarization from SMBHB merging at NGC 6240 ($D_L = 111.2$ Mpc) for the last 50 yr (left) and last 10 yr (right). Major merging is represented by binary component with masses $1.36 \times 10^9 M_\odot$ and $6.8 \times 10^8 M_\odot$ and corresponding mass ratio 2:1. The final separation (due to our \mathcal{PN} routine) is 0.75 mpc. The solid vertical line on the left-hand panel indicates the last 10 yr of merging. Dashed vertical lines from left to right indicate binary separation 15, 10, and 5 Schwarzschild radii, respectively.

REFERENCES

- Andonie C. et al., 2022, *A&A*, 664, A46
 Arzoumanian Z. et al., 2020, *ApJ*, 905, L34
 Avramov B., Berczik P., Meiron Y., Acharya A., Just A., 2021, *A&A*, 649, A41
 Barausse E., 2012, *MNRAS*, 423, 2533
 Barger A. J., Cowie L. L., Sanders D. B., Fulton E., Taniguchi Y., Sato Y., Kawara K., Okuda H., 1998, *Nature*, 394, 248
 Barret D. et al., 2018, in den Herder J.-W. A., Nikzad S., Nakazawa K., eds, Proc. SPIE Conf. Ser. Vol. 10699, Space Telescopes and Instrumentation 2018: Ultraviolet to Gamma Ray. SPIE, Bellingham, p. 106991G
 Begelman M. C., Blandford R. D., Rees M. J., 1980, *Nature*, 287, 307
 Bennett C. L. et al., 2003, *ApJS*, 148, 1
 Berczik P., Merritt D., Spurzem R., Bischof H.-P., 2006, *ApJ*, 642, L21
 Berczik P. et al., 2011, in Sergienko I. V., ed., International conference on High Performance Computing, Kyiv, Ukraine. NASU, p. 8
 Berentzen I., Preto M., Berczik P., Merritt D., Spurzem R., 2008, *Astron. Nachr.*, 329, 904
 Berentzen I., Preto M., Berczik P., Merritt D., Spurzem R., 2009, *ApJ*, 695, 455
 Beswick R. J., Pedlar A., Mundell C. G., Gallimore J. F., 2001, *MNRAS*, 325, 151
 Blanchet L., 2006, *Living Rev. Relativ.*, 9, 4
 Blumenthal G. R., Faber S. M., Primack J. R., Rees M. J., 1984, *Nature*, 311, 517
 Bortolas E., Franchini A., Bonetti M., Sesana A., 2021, *ApJ*, 918, L15
 Brem P., Amaro-Seoane P., Spurzem R., 2013, *MNRAS*, 434, 2999
 Campanelli M., Lousto C. O., Zlochower Y., Merritt D., 2007, *Phys. Rev. Lett.*, 98, 231102
 Carter C., Karovska M., Jerius D., Glotfelty K., Beikman S., 2003, in Payne H. E., Jędrzejewski R. I., Hook R. N., eds, ASP Conf. Ser. Vol. 295, Astronomical Data Analysis Software and Systems XII. Astron. Soc. Pac., San Francisco, p. 477
 Choi D.-I., Kelly B. J., Boggs W. D., Baker J. G., Centrella J., van Meter J., 2007, *Phys. Rev. D*, 76, 104026
 Cuadra J., Armitage P. J., Alexander R. D., Begelman M. C., 2009, *MNRAS*, 393, 1423
 Dehnen W., 1993, *MNRAS*, 265, 250
 Dobrycheva D. V., Vavilova I. B., Melnyk O. V., Elyiv A. A., 2018, *Kinematics Phys. Celest. Bodies*, 34, 290
 Engel H. et al., 2010, *A&A*, 524, A56
 Fabbiano G., Paggi A., Karovska M., Elvis M., Nardini E., Wang J., 2020, *ApJ*, 902, 49
 Ferrarese L., Merritt D., 2000, *ApJ*, 539, L9
 Fiestas J., Porth O., Berczik P., Spurzem R., 2012, *MNRAS*, 419, 57
 Freeman P., Doe S., Siemiginowska A., 2001, in Starck J.-L., Murtagh F. D., eds, SPIE Conference series, Vol. 4477, Astronomical Data Analysis. SPIE, Bellingham, p. 76.
 Fruscione A. et al., 2006, in Silva D. R., Doxsey R. E., eds, SPIE Conference series, Vol. 6270, Observatory Operations: Strategies, Processes, and Systems. SPIE, Bellingham, p. 62701V
 Fyhrie A., Glenn J., Rangwala N., Wheeler J., Beck S., Bally J., 2021, *ApJ*, 922, 208
 Gallimore J. F., Beswick R., 2004, *AJ*, 127, 239
 Gaskin J. A. et al., 2019, *J. Astron. Telesc. Instrum. Syst.*, 5, 021001
 Gerssen J., van der Marel R. P., Axon D., Mihos J. C., Hernquist L., Barnes J. E., 2004, *AJ*, 127, 75
 González J. A., Hannam M., Sperhake U., Brüggmann B., Husa S., 2007, *Phys. Rev. Lett.*, 98, 231101
 Gröbner M., Ishibashi W., Tiwari S., Haney M., Jetzer P., 2020, *A&A*, 638, A119
 Haardt F., Maraschi L., 1991, *ApJ*, 380, L51
 Haardt F., Maraschi L., 1993, *ApJ*, 413, 507
 Haehnelt M. G., 1994, in Courvoisier T., Blecha A., eds, IAU Symp., Vol. 159, Multi-Wavelength Continuum Emission of AGN. Kluwer Academic Publishers, p. 279
 Hagiwara Y., Diamond P. J., Miyoshi M., 2002, *A&A*, 383, 65
 Hagiwara Y., Diamond P. J., Miyoshi M., 2003, *A&A*, 400, 457
 Hagiwara Y., Baan W. A., Klöckner H.-R., 2011, *AJ*, 142, 17
 Hénon M. H., 1971, *Ap&SS*, 14, 151
 Hernquist L., 1990, *ApJ*, 356, 359
 Hobbs G., 2013, *Class. Quantum Gravity*, 30, 224007
 Husemann B., Heidt J., De Rosa A., Vignali C., Bianchi S., Bogdanović T., Komossa S., Paragi Z., 2020, *A&A*, 639, A117
 Iono D. et al., 2007, *ApJ*, 659, 283
 Jaffe W., 1983, *MNRAS*, 202, 995
 Kauffmann G., Colberg J. M., Diaferio A., White S. D. M., 1999, *MNRAS*, 303, 188
 Khan F. M., Fiacconi D., Mayer L., Berczik P., Just A., 2016, *ApJ*, 828, 73
 Khan F. M., Berczik P., Just A., 2018a, *A&A*, 615, A71
 Khan F. M., Capelo P. R., Mayer L., Berczik P., 2018b, *ApJ*, 868, 97

- Kidder L. E., 1995, *Phys. Rev. D*, 52, 821
- Kollatschny W., Weillbacher P. M., Ochmann M. W., Chelouche D., Monreal-Ibero A., Bacon R., Contini T., 2020, *A&A*, 633, A79
- Komossa S., Burwitz V., Hasinger G., Predehl P., Kaastra J. S., Ikebe Y., 2003, *ApJ*, 582, L15
- Kompaniets O. V., Vasylenko A. A., 2020, *Astrophysics*, 63, 307
- Kormendy J., Ho L. C., 2013, *ARA&A*, 51, 511
- Kormendy J., Richstone D., 1995, *ARA&A*, 33, 581
- Kramer M., Champion D. J., 2013, *Class. Quantum Gravity*, 30, 224009
- Kupi G., Amaro-Seoane P., Spurzem R., 2006, *MNRAS*, 371, L45
- Le Tiec A., 2014, *Int. J. Mod. Phys. D*, 23, 1430022
- Li S., Liu F. K., Berczik P., Chen X., Spurzem R., 2012, *ApJ*, 748, 65
- Lodato G., Nayakshin S., King A. R., Pringle J. E., 2009, *MNRAS*, 398, 1392
- Manchester R. N., IPTA, 2013, *Class. Quantum Gravity*, 30, 224010
- Matt G., Perola G. C., Piro L., 1991, *A&A*, 247, 25
- Maureira-Fredes C., Goicovic F. G., Amaro-Seoane P., Sesana A., 2018, *MNRAS*, 478, 1726
- Medling A. M., Ammons S. M., Max C. E., Davies R. I., Engel H., Canalizo G., 2011, *ApJ*, 743, 32
- Menci N., Cavaliere A., Fontana A., Giallongo E., Poli F., 2002, *ApJ*, 575, 18
- Merritt D., 2001, *ApJ*, 556, 245
- Merritt D., Ferrarese L., 2001, *MNRAS*, 320, L30
- Milosavljević M., Merritt D., 2003a, *ApJ*, 596, 860
- Milosavljević M., Merritt D., 2003b, in Centrella J. M., ed., AIP Conf. Ser. Vol. 686, The Astrophysics of Gravitational Wave Sources. Am. Inst. Phys., New York, p. 201
- Müller-Sánchez F., Nevin R., Comerford J. M., Davies R. I., Privon G. C., Treister E., 2018, *Nature*, 556, 345
- Mushotzky R. F., Done C., Pounds K. A., 1993, *ARA&A*, 31, 717
- Nandra K., 2006, *MNRAS*, 368, L62
- Nandra K. et al., 2013, preprint ([arXiv:1306.2307](https://arxiv.org/abs/1306.2307))
- Nardini E., 2017, *MNRAS*, 471, 3483
- Nasim I., Gualandris A., Read J., Dehnen W., Delorme M., Antonini F., 2020, *MNRAS*, 497, 739
- Pasquali A., de Grijs R., Gallagher J. S., 2003, *MNRAS*, 345, 161
- Perets H. B., Hopman C., Alexander T., 2007, *ApJ*, 656, 709
- Peters P. C., 1964a, PhD thesis, California Institute of Technology
- Peters P. C., 1964b, *Phys. Rev.*, 136, 1224
- Peters P. C., Mathews J., 1963, *Phys. Rev.*, 131, 435
- Pignata G. et al., 2010, Cent. Bur. Electron. Telegrams, 1, 2591
- Plummer H. C., 1911, *MNRAS*, 71, 460
- Preto M., Berentzen I., Berczik P., Spurzem R., 2011, *ApJ*, 732, L26
- Puccetti S. et al., 2016, *A&A*, 585, A157
- Quinlan G. D., 1996, *New Astron.*, 1, 35
- Ransom S. et al., 2019, in Bulletin of the American Astronomical Society, Vol. 51, 7, p. 195, preprint ([arXiv:1908.05356](https://arxiv.org/abs/1908.05356))
- Rantala A., Pihajoki P., Johansson P. H., Naab T., Lahén N., Sawala T., 2017, *ApJ*, 840, 53
- Reisswig C., Husa S., Rezzolla L., Dorband E. N., Pollney D., Seiler J., 2009, *Phys. Rev. D*, 80, 124026
- Ricci C., Ueda Y., Ichikawa K., Paltani S., Boissay R., Gandhi P., Stalewski M., Awaki H., 2014, *A&A*, 567, A142
- Richstone D. et al., 1998, *Nature*, 385, A14
- Rybicki G. B., Lightman A. P., 1979, Radiative Processes in Astrophysics. A Wiley-Interscience Publication, New York
- Sanders D. B., Mazzarella J. M., Kim D. C., Surace J. A., Soifer B. T., 2003, *AJ*, 126, 1607
- Sobolenko M., Berczik P., Spurzem R., 2016, in Meiron Y., Li S., Liu F. K., Spurzem R., eds, Proc. IAU Symp. Vol. 312, Star Clusters and Black Holes in Galaxies across Cosmic Time. Cambridge University Press, Cambridge, p. 105
- Sobolenko M., Berczik P., Spurzem R., Kupi G., 2017, *Kinematics Phys. Celest. Bodies*, 33, 21
- Sobolenko M., Berczik P., Spurzem R., 2021, *A&A*, 652, A134 (S21)
- The Lynx Team, 2018, preprint ([arXiv:1809.09642](https://arxiv.org/abs/1809.09642))
- Treister E. et al., 2020, *ApJ*, 890, 149
- Tremaine S. et al., 2002, *ApJ*, 574, 740
- Vasylenko A. A., 2018, *Ap&SS*, 363, 228
- Vavilova I. B. et al., 2015, Dark Matter: Observational Manifestation and Experimental Searches. Akadempriodyka, Kyiv
- Wang L., Berczik P., Spurzem R., Kouwenhoven M. B. N., 2014a, *ApJ*, 780, 164
- Wang J. et al., 2014b, *ApJ*, 781, 55
- White S. D. M., Rees M. J., 1978, *MNRAS*, 183, 341
- Wise M., 1997, *Chandra News*, 5, 22
- Wright E. L., 2006, *PASP*, 118, 1711
- Wyithe J. S. B., Loeb A., 2003, *ApJ*, 590, 691
- Yu Q., 2002, *MNRAS*, 331, 935
- Zhong S., Berczik P., Spurzem R., 2014, *ApJ*, 792, 137
- Zoldan A., De Lucia G., Xie L., Fontanot F., Hirschmann M., 2019, *MNRAS*, 487, 5649

This paper has been typeset from a $\text{\TeX}/\text{\LaTeX}$ file prepared by the author.